AIAA JOURNAL
Vol. 44, No. 7, July 2006

Flutter/Limit Cycle Oscillation Analysis and Experiment for Wing-Store Model

Deman Tang,* Peter Attar,† and Earl H. Dowell‡
Duke University, Durham, North Carolina 27708-0300

A delta wing experimental model with an external store has been designed and tested in the Duke University wind tunnel. The wing structure is modeled theoretically by using von Kármán plate theory that allows for geometric strain-displacement nonlinearities in the plate wing structure. A component modal analysis is used to derive the full structural equations of motion for the wing/store combination system. A three-dimensional time domain vortex lattice aerodynamic model including a reduced-order model aerodynamic technique and a slender-body aerodynamic theory for the store are also used to investigate the nonlinear aeroelastic system. The effects of the store pitch stiffness (attachment stiffness), the span location of store, and the store aerodynamics on the critical flutter velocity and limit cycle oscillations (LCO) are discussed. The correlations between the theory and experiment are good for both the critical flutter velocity and frequency but not good for the LCO amplitude, especially when the store is located near the wing tip. The theoretical structural model needs to be improved to determine LCO response, and improved results are shown in the companion paper as obtained with a higher-order structural model.

Nomenclature

a_i, b_j	=	generalized coordinates in x, y directions, respectively
c	=	delta wing root chord
D	=	delta wing plate bending stiffness
E	=	Young's modulus
h	=	delta wing plate thickness
km, kn	=	numbers of vortex elements on delta wing in x, y directions, respectively
kmm	=	total number of vortices on both the delta wing and wake in the x direction
L	=	delta wing span; also lift on the slender body
M_y, M_β	=	aerodynamic moment
m	=	delta wing panel mass/area, $m = h\rho_m$
mxy	=	number of structural modal functions in the x, y plane defining u, v
nxy	=	number of structural modal functions in the z direction defining w
Q^{ij}	=	generalized aerodynamic force
$\boldsymbol{q}, \dot{\boldsymbol{q}}$	=	state-space vector
q_n	=	generalized coordinate in the z direction
R_a	=	size of reduced-order aerodynamic model
t	=	time
U	=	airspeed
U_f	=	critical flutter velocity
U_i, V_j	=	modal functions in x, y directions
u, v	=	in-plane displacements
w	=	plate transverse deflection
X, Y	=	right and left eigenvector matrices of vortex lattice eigenvalue model
x, y	=	streamwise and spanwise coordinates
Z	=	eigenvalue matrix of vortex lattice aerodynamic model
z	=	normal coordinate
β	=	store pitch angle
Γ	=	vortex strength
γ	=	vortex strength modal amplitudes
$\underline{\Delta p}$	=	aerodynamic pressure loading on panel
$\overline{\Delta p}$	=	nondimensional aerodynamic pressure, $\Delta p/(\rho_\infty U^2)$
Δt	=	integration time step
Δx	=	plate element length in the streamwise direction
θ	=	state-space vector of structural deformation
ν	=	Poisson's ratio
ρ_∞, ρ_m	=	air and plate densities
τ	=	time parameter, $\sqrt{(mc^4/D)}$, s
ψ_k	=	transverse modal function in z direction
ω	=	frequency
$(\dot{})$	=	$\mathrm{d}(\,)/\mathrm{d}t$

Received 3 August 2004; accepted for publication 30 June 2005.

*Research Associate Professor, Department of Mechanical Engineering and Materials Science. Member AIAA.

†Postdoctoral Fellow, Department of Mechanical Engineering and Materials Science. Member AIAA.

‡William Holland Hall Professor, Department of Mechanical Engineering and Materials Science, and Director, Center for Nonlinear and Complex Systems. Member AIAA.

I. Introduction

A WING with an external store is a common configuration for military aircraft. A limit cycle oscillation (LCO) has been observed in both theoretical models and flight tests. However, the precipitating physical mechanism remains to be fully understood. Fundamentally LCO is a limited-amplitude, self-sustaining oscillation produced by structural and aerodynamic interaction. LCO may occur because of the interaction of linear structural response and nonlinear aerodynamic forces due to transonic shock oscillation and shock-induced flow separation on the wing trailing edge. Another possible cause of LCO is the structural nonlinearity at the attachment between the wing and the store, i.e., a freeplay gap and/or dry friction damping in the bolt connection. Also, the wing geometric structural nonlinearity is another possible source for the LCO when a sufficiently large deflection occurs.

For the present studies, a delta wing experimental model with an external store model has been designed. The wing is modeled as a simple plate of constant thickness. The store is modeled as a slender rigid body that contacts the wing through two support points. The fore support point is articulated to the wing, and the aft support point contacts the wing through a spring and freeplay gap. The store is assumed to have motion relative to the wing in only one degree of freedom, i.e., in pitch. Thus the store itself is a single-degree-of-freedom system excited by nonlinear forces from the wing through the two support points.

For the plate delta wing alone, theoretical and experimental results[1–4] have provided a good physical understanding of the flutter and LCO characteristics. Also see the interesting work of Gordnier.[5] In particular, it has been demonstrated that even with only a single edge (root) of a plate restrained, bending-tension or geometrical nonlinearities can produce LCO amplitudes of the order of several plate thicknesses. Changes in the limit cycle and flutter behavior as the angle of attack is varied also have been observed in both the theoretical predictions and wind-tunnel tests. The results do show that a change in the aeroelastic behavior at angle of attack can be caused by a structural nonlinearity as well as a fluid nonlinearity.

In this paper, the wing is modeled by using von Kármán plate theory that allows for geometric strain-displacement nonlinearities in the plate wing structure. A component modal analysis[6,7] is used to derive the full structural equations of motion for the wing/store combination system. A three-dimensional time domain vortex lattice aerodynamic model using a reduced-order model aerodynamic technique[8] and a slender-body aerodynamic theory for the store are also used to investigate the nonlinear aeroelastic system.

To evaluate the theoretically predicted flutter and LCO characteristics of the delta wing/store model, an experimental investigation has been carried out in the Duke University wind tunnel using an Ometron VPI 4000 Scanning Laser Vibrometer system to measure deflections (velocities) of the delta wing and store. The VPI sensor is a noncontacting transducer that uses optical interferometry and electronic frequency measurements to determine the frequency shift of a beam of light reflected from a moving surface.

II. State-Space Equations of Motion

A schematic of the delta wing-plate/store geometry is shown in Fig. 1, and a photograph of the experimental delta wing-plate/store model in the wind tunnel is shown in Fig. 2. The aeroelastic structure/fluid state-space equations are described next.

A. Nonlinear Structural Model

The plate wing and store structures can be viewed as separate components that can be analyzed individually and then joined through an appropriate constraint function. The full structural equations of motion can thus be obtained in a very compact form. First, the kinetic and potential energies of the plate wing based on the von Kármán plate theory are discussed.

The elastic strain energy of the plate is as follows:

$$V^p = \frac{D}{2}\iint \left[(w_{xx})^2 + (w_{yy})^2 + 2\nu w_{xx}w_{yy} + 2(1-\nu)(w_{xy})^2\right] \times \mathrm{d}x\,\mathrm{d}y + \frac{Eh}{2(1-\nu^2)}\iint \left\{\left[u_x + \frac{1}{2}(w_x)^2\right]^2 + \left[v_y + \frac{1}{2}(w_y)^2\right]^2\right\}\mathrm{d}x\,\mathrm{d}y + \frac{Eh}{2(1-\nu^2)}\iint 2\nu \times \left[u_x + \frac{1}{2}(w_x)^2\right]\left[v_y + \frac{1}{2}(w_y)^2\right]\mathrm{d}x\,\mathrm{d}y + \frac{Eh}{2(1-\nu^2)} \times \iint \frac{(1-\nu)}{2}[v_x + u_y + w_x w_y]^2\,\mathrm{d}x\,\mathrm{d}y + \iint m_p g w\,\mathrm{d}x\,\mathrm{d}y \tag{1}$$

where $w_x \equiv \partial w/\partial x$, $w_{xy} \equiv \partial^2 w/\partial x\,\partial y$, and similar expressions hold for $u_x, u_y, v_x \ldots$.

The kinetic energy of a plate, ignoring the in-plane inertia, is

$$T^p = \frac{1}{2}\iint m_p(\dot{w})^2\,\mathrm{d}x\,\mathrm{d}y \tag{2}$$

In Eq. (1) the first double integral is the strain energy from linear plate theory. The next three integrals are the additional strain energy contributions if one includes second-order terms in the strain-displacement relations. The last integral in Eq. (1) is the potential energy due to gravity.

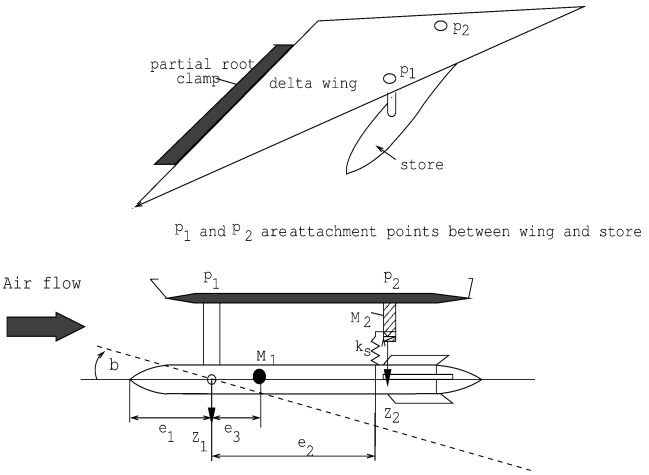

Fig. 1 Delta wing model with an external store in the wind tunnel.

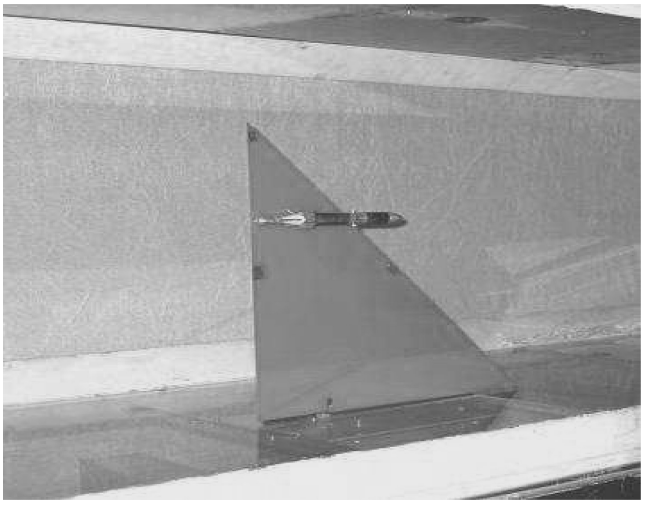

Fig. 2 Photograph of the experimental delta wing model with an external store in the wind tunnel.

The classical Rayleigh–Ritz approach is used here. In the Rayleigh–Ritz approach the original displacement variables u, v, w, which are functions of x, y, and t, are expanded in a series of the product of time-dependent modal coordinates and space-dependent global functions. We expand the transverse or out-of-plane displacement w and the in-plane displacements u and v as follows:

$$u(x,y,t) = \sum_m a_m(t)U_m(x,y), \qquad m = 1 \ldots mxy \tag{3}$$

$$v(x,y,t) = \sum_n b_n(t)V_n(x,y), \qquad n = 1 \ldots mxy \tag{4}$$

$$w(x,y,t) = \sum_k q_k(t)\psi_k(x,y), \qquad k = 1 \ldots nxy \tag{5}$$

where the transverse natural mode function $\psi_k(x,y)$ is calculated by using a two-dimensional finite element method for the delta wing plate. The in-plane natural mode functions $U_i(x,y)$ and $V_j(x,y)$ are calculated by a three-dimensional finite element method. All such calculations are done by using a standard computational code, ANSYS.[9] These functions satisfy the boundary conditions (partial root clamp) of the cantilevered delta wing.

1. *Delta Wing Plate Energies and Virtual Work*

Substituting Eqs. (3–5) into Eqs. (1) and (2) and using the mode orthogonality condition, the potential energy of the wing plate is

expressed as

$$V^p = \frac{1}{2}\sum_{k=1}^{nxy} m_k\omega_k^2 q_k^2 + \sum_{k=1}^{nxy}\sum_{m=1}^{mxy}\sum_{l=1}^{nxy} S^a_{lmk} a_m q_l q_k + \sum_{k=1}^{nxy}\sum_{n=1}^{mxy}\sum_{l=1}^{nxy} \times S^b_{lnk} b_n q_l q_k \sum_{k=1}^{nxy}\sum_{r=1}^{nxy}\sum_{s=1}^{nxy}\sum_{t=1}^{nxy} S^q_{rstk} q_r q_s q_t q_k + \sum_{k=1}^{nxy} S^{mg}_k q_k \quad (6)$$

and the kinetic energy is

$$T^p = \frac{1}{2}\sum_{k=1}^{nxy} m_k \dot{q}_k^2 \quad (7)$$

where m_k, ω_k are the generalized mass and natural frequency of the delta wing associated with the kth eigenmode. The last term of Eq. (6) comprises the potential energy due to gravity.

The generalized nonconservative work for the wing plate can be expressed as

$$\delta W^p = \sum_{p=1}^{NN}\sum_{k=1}^{nxy} \Delta P_p \psi_k \delta q_k + \sum_{k=1}^{nxy} F^\beta \psi_k(p_1)\delta q_k \quad (8)$$

where ΔP_p is the aerodynamic pressure loading on pth panel that is used to discretely describe the surface of the wing. F^β is the out-of-plane(z) force loading on the aft attachment point p_1 of the store.

2. Store Energies and Virtual Work

The potential energy of the store is expressed as

$$V^\beta = \tfrac{1}{2}k_s(Z_1 + \beta e_2 - Z_2)^2 + (M_1 Z_1 + M_2 Z_2)g + M_1 g\beta e_3 \quad (9)$$

where k_s is the attachment stiffness between the wing and store at the aft attached point.

The kinetic energy of the store is

$$T^\beta = \tfrac{1}{2}\left(M_1\dot{Z}_1^2 + M_2\dot{Z}_2^2 + J_\beta\dot{\beta}^2\right) \quad (10)$$

The generalized nonconservative work for the store can be expressed as

$$\delta W^\beta = M^\beta \delta\beta \quad (11)$$

In Eqs. (9–11) M_1 is the mass of the store and M_2 is the mass of the aft attachment point; Z_1 and Z_2 are the displacements of the fore and aft attachment points of the store, respectively; (p_1) (fore) and (p_2) (aft) are the attachment points between the wing and the store; and e_2 and e_3 are the distances between fore and aft attachment points of the store and between the fore attachment point and the mass center of the store, respectively. M^β is an aerodynamic moment loading on the store. The last two terms of Eq. (9) comprise the potential energy due to gravity.

The constraint conditions at the fore and aft attached points between the wing and the store may be expressed as

$$f_1 \equiv \sum_{k=1}^{nxy} q_k\psi_k(p_1) - Z_1 = 0 \quad (12)$$

$$f_2 \equiv \sum_{k=1}^{nxy} q_k\psi_k(p_2) - Z_2 = 0 \quad (13)$$

The Lagrangian is

$$L = T - V + \sum_{i=1}^{2}\lambda_i f_i = T^p + T^\beta - V^p - V^\beta + \lambda_1 f_1 + \lambda_2 f_2$$

where λ_i are Lagrange multipliers.

Lagrange's equations for this system are derived with respect to q_k, Z_1, Z_2, λ_1, λ_2, and β, i.e.,

$$m_k\left[\ddot{q}_k + \omega_k^2 q_k\right] - F_g^k - Q^k - F^\beta + F_N^k = \lambda_1\psi_k(p_1) + \lambda_2\psi_k(p_2) \quad (14)$$

$$M_1\ddot{Z}_1 + k_s(Z_1 - Z_2 + e_2\beta) - M_1 g = -\lambda_1 \quad (15)$$

$$M_2\ddot{Z}_2 + k_s(Z_2 - Z_1 - e_2\beta) - M_2 g = -\lambda_2 \quad (16)$$

$$J_\beta\ddot{\beta} + k_s e_2^2\beta + k_s e_2(Z_1 - Z_2) - M^\beta - M_1 e_3 g = 0 \quad (17)$$

$$\sum_{k=1}^{nxy} q_k\psi_k(p_1) - Z_1 = 0 \quad (18)$$

$$\sum_{k=1}^{nxy} q_k\psi_k(p_2) - Z_2 = 0 \quad (19)$$

where F_N^k is a nonlinear force that depends on the deflection of wing, i.e.,

$$F_N^k = \sum_{m=1}^{mxy}\sum_{l=1}^{nxy} a_m q_l K1_{mlk} + \sum_{n=1}^{mxy}\sum_{l=1}^{nxy} b_n q_l K2_{nlk} + \sum_{r=1}^{nxy}\sum_{s=1}^{nxy}\sum_{t=1}^{nxy} q_r q_s q_t K3_{rstk}$$

Q^k, F^β, and M^β are the generalized aerodynamic forces loading on the wing plate and on the store; F_g^k, $M_1 g$, $M_2 g$, and $M_1 e_3 g$ are the generalized gravity forces loading on the wing plate and on the store.

Eliminating Z_1, Z_2, λ_1, and λ_2, from these equations, one obtains

$$m_k\ddot{q}_k + M_1\psi_k(p_1)\sum_{k=1}^{nxy}\ddot{q}_k\psi_k(p_1) + M_2\psi_k(p_2)\sum_{k=1}^{nxy}\ddot{q}_k\psi_k(p_2) + m_k\omega_k^2 q_k + k_s\Delta\psi_k\left[\sum_{k=1}^{nxy} q_k\Delta\psi_k - e_2\beta\right] = Q^k - F_N^k + F^\beta\psi_k(p_1) + F_g^k + [M_1\psi_k(p_1) + M_2\psi_k(p_2)]g \quad k = 1\ldots nxy \quad (20)$$

$$J_\beta\ddot{\beta} + k_s e_2^2\beta - k_s e_2\sum_{k=1}^{nxy} q_k\Delta\psi_k = M^\beta + M_1 e_3 \quad (21)$$

where $\Delta\psi_k \equiv \psi_k(p_2) - \psi_k(p_1)$.

Lagrange's equations for this system are also derived with respect to a_m, b_n, i.e.,

$$\sum_{i=1}^{mxy} a_i A1_{im} + \sum_{j=1}^{mxy} b_j B1_{jm} = \sum_{l=1}^{nxy}\sum_{o=1}^{nxy} q_l q_k C1_{lkm} \quad m = 1\ldots mxy \quad (22)$$

$$\sum_{i=1}^{mxy} a_i A2_{in} + \sum_{j=1}^{mxy} b_j B2_{jn} = \sum_{l=1}^{nxy}\sum_{o=1}^{nxy} q_l q_k C2_{lkn} \quad n = 1\ldots mxy \quad (23)$$

Note that the store (slender body) drag is neglected in the present analysis.

B. Aerodynamic Model

1. Vortex Lattice Model for the Delta Wing

The flow about the wing/store is assumed to be incompressible, inviscid, and irrotational. Here we use an unsteady vortex lattice

method to model this flow. The plate and wake are divided into a number of elements. In the wake and on the wing, all of the elements are of equal size, Δx, in the streamwise direction. Point vortices are placed on the plate and in the wake at the quarter chord of the elements. At the three-quarter chord of each plate element a collocation point is placed for the downwash, i.e., the velocity induced by the discrete vortices is set equal to the downwash arising from the unsteady motion of the delta wing. Thus we have the relationship

$$w_i^{t+1} = \sum_{j}^{kmm} K_{ij}\Gamma_j^{t+1}, \qquad i = 1, \ldots km \tag{24}$$

where w_i^{t+1} is the downwash at the ith collocation point at time step $t+1$, Γ_j is the strength of the jth vortex, and K_{ij} is an aerodynamic kernel function.

An aerodynamic matrix equation is then formed:

$$[A]\{\Gamma\}^{t+1} + [B]\{\Gamma\}^{t} = \{w\}^{t+1} \tag{25}$$

where $[A]$ and $[B]$ are aerodynamic coefficient matrices.[2–4]

From the fundamental aerodynamic theory, we can obtain the pressure distribution on the plate at the jth point in terms of the vortex strengths. The aerodynamic pressure is given by

$$\Delta p_j = \frac{\rho_\infty}{\Delta x}\left[U\left(\Gamma_j^{t+1} + \Gamma_j^{t}\right)/2 + \sum_{i}^{j} \Delta x\left(\Gamma_i^{t+1} - \Gamma_i^{t}\right)/\Delta t\right] \tag{26}$$

and the aerodynamic generalized force is calculated from

$$Q^k = \iint \Delta p \psi_k \, \mathrm{d}x \, \mathrm{d}y = \sum_{j=1}^{NN} \Delta p_j \psi_k(x_j, y_j)\Delta x \Delta y \tag{27}$$

2. Slender Body Model for the Store

We follow Bisplinghoff et al. (Ref. 10, p. 418 et seq) and for clarity use their equation numbers. By using essentially the nomenclature of Ref. 10, we define $h = Z_1$, $\alpha = \beta$, $L = F^\beta$, and $M_y = M^\beta$ but use the symbol x_β to denote chordwise position. Then the vertical displacement at any point of the store is

$$Z_a = -h - \alpha[x_\beta - e_1] \tag{7-136}$$

where $x_B \equiv e_1$, is the distance from the leading edge to the elastic axis of the slender body. Here h, + up, and α, + nose up. Now the downwash or convected vertical velocity is

$$w_a(x_\beta, t) = \frac{\partial Z_a}{\partial t} + U\frac{\partial Z_a}{\partial x_\beta} \tag{7-137}$$

Thus from Ref. 9,

$$\frac{dL}{dx_\beta} = -\rho_\infty \frac{DS}{Dt}\left[\frac{\partial Z_a}{\partial t} + U\frac{\partial Z_a}{\partial x_\beta}\right] - \rho_\infty S\left[\frac{D}{Dt}\left(\frac{\partial Z_a}{\partial t}\right) + U\frac{D}{Dt}\left(\frac{\partial Z_a}{\partial x_\beta}\right)\right] \tag{7-140}$$

where $D/Dt \equiv \partial/\partial t + U(\partial/\partial x_\beta)$, $S \equiv$ body cross-sectional area, and $S = \pi R^2$, for a circular cross section of radius $R(x_\beta)$. Note that

$$\frac{DS}{Dt} = U\frac{dS}{dx_\beta} \tag{7-142}$$

Then Eq. (7-140) becomes

$$\frac{dL}{dx_\beta} = -\rho U\frac{dS}{dx_\beta}\frac{DZ_a}{Dt} - \rho S\frac{D^2 Z_a}{Dt^2} \tag{7-143}$$

Now,

$$L \equiv \int_0^{c_{SB}} \frac{dL}{dx_\beta} dx_\beta$$

and

$$M_y \equiv \int_0^{c_{SB}} \frac{dL}{dx_\beta}[x_\beta - e_1]dx_\beta$$

where $c_{SB} \equiv$ chord of the slender body.

Using Eq. (7-136),

$$\frac{DZ_a}{Dt} = -\dot{h} - \dot{\alpha}[x_\beta - e_1] - U\alpha$$

$$\frac{D^2 Z_a}{D^2 t} = -\ddot{h} - \ddot{\alpha}[x_\beta - e_1] - 2U\dot{\alpha}$$

thus

$$F^\beta \equiv L = \int_0^{c_{SB}} \frac{dL}{dx_\beta}dx_\beta = \rho[\ddot{h} + U\dot{\alpha}]\int_0^{c_{SB}} S dx_\beta + \rho\ddot{\alpha}\int_0^{c_{SB}} S[x_\beta - e_1]dx_\beta \tag{8-1}$$

$$M^\beta \equiv M_y = \rho U[\dot{h} + U\alpha]\int_0^{c_{SB}} S dx_\beta - \rho\ddot{h}\int_0^{c_{SB}} S[x_\beta - e_1]dx_\beta - \rho\ddot{\alpha}\int_0^{c_{SB}} S[x_\beta - e_1]^2 dx_\beta \tag{11-1}$$

Note that

$$\int_0^{c_{SB}} \frac{dS}{dx_\beta}dx_\beta = 0$$

if $S = 0$ at $x_\beta = 0$, c_{SB}, i.e., for bodies closed at both ends.

Also, recall that the sign convention is x_β, positive aft; L, positive up; and M_y, positive nose up.

C. Aeroelastic State-Space Equations

Consider a discrete time history of the delta wing, $q(t)$, and the store, $\beta(t)$, with a constant sampling time step Δt. The structural dynamic equations (20–22) can be reconstituted as a state-space equation in discrete time form, i.e.,

$$[D_2]\{\theta\}^{t+1} + [D_1]\{\theta\}^{t} + [C_2]\{\Gamma\}^{t+1} + [C_1]\{\Gamma\}^{t} = -\left\{F_N^p\right\}^{t+\frac{1}{2}} + \{F_g\} \tag{28}$$

where the vector $\{\theta\}$ is the state of the plate and $\{\theta\} = \{\dot{q}, \dot{\beta}, q, \beta\}$ and $[D_1]$, $[D_2]$ are matrices describing the wing plate and store structural behavior. $[C_1]$, $[C_2]$ are matrices describing the vortex element behavior on the delta wing itself. $\{F_N^p\}$ is the nonlinear force matrix generated by the wing plate structural nonlinearity. $\{F_g\}$ is a static force matrix due to gravity.

There is a linear relationship between the downwash w at the collocation points and delta wing response $\{\theta\}$. It is defined by

$$\{w\} = [E]\{\theta\} \tag{29}$$

Thus, combining Eqs. (26), (29), and (30), we obtain a complete aeroelastic state-space equation in matrix form:

$$\begin{bmatrix} A & -E \\ C_2 & D_2 \end{bmatrix}\begin{Bmatrix} \Gamma \\ \theta \end{Bmatrix}^{t+1} + \begin{bmatrix} B & 0 \\ C_1 & D_1 \end{bmatrix}\begin{Bmatrix} \Gamma \\ \theta \end{Bmatrix}^{t} = \begin{Bmatrix} 0 \\ -F_N^p + F_g \end{Bmatrix}^{t+\frac{1}{2}} \tag{30}$$

III. Reduced-Order Aerodynamic Model

The vortex lattice aerodynamic model may be "reduced" by using aerodynamic eigenmodes.[2–4,8] To accomplish this, a transformation from the original flow variables $\{\Gamma\}$ to the modal variables $\{\gamma\}$ is made:

$$\{\Gamma\} = \left[X_{R_a}\right]\{\gamma\} \tag{31}$$

where X_{R_a} is right eigenvectors and R_a is the number of aerodynamic modal vectors kept in the matrix of aerodynamic eigenvectors X. In practice R_a is much less than the dimension of the full vortex lattice model; $\{\gamma\}$ is the vector of the aerodynamic modal coordinates.

Thus the reduced aeroelastic model has the form[2]

$$\begin{bmatrix} I & -Y_{R_a}^T E \\ C_2 X_{R_a} & D_2 \end{bmatrix} \begin{Bmatrix} \gamma \\ \theta \end{Bmatrix}^{t+1} + \begin{bmatrix} -Z_{R_a} & 0 \\ C_1 X_{R_a} & D_1 \end{bmatrix} \begin{Bmatrix} \gamma \\ \theta \end{Bmatrix}^{t}$$

$$= \begin{Bmatrix} 0 \\ -F_N^p + F_g \end{Bmatrix}^{t+\frac{1}{2}} \tag{32}$$

To account for the neglected aerodynamic eigenmodes, we use a quasi-static correction that accounts for much of their influence. This technique is similar to the mode-acceleration method common to structural dynamics. Finally, the reduced-order model with static correction is given by

$$\begin{bmatrix} I & -Y_{R_a}^T [I - A(A+B)^{-1}]E \\ C_2 X_{R_a} & D_2 + (C_2(A+B)^{-1}E \end{bmatrix} \begin{Bmatrix} \gamma_d \\ \theta \end{Bmatrix}^{t+1}$$

$$+ \begin{bmatrix} -Z_{R_a} & -Y_{R_a}^T B(A+B)^{-1}E \\ C_1 X_{R_a} & D_1 + C_1(A+B)^{-1}E \end{bmatrix} \begin{Bmatrix} \gamma_d \\ \theta \end{Bmatrix}^{t}$$

$$= \begin{Bmatrix} 0 \\ -F_N^p + F_g \end{Bmatrix}^{t+\frac{1}{2}} \tag{33}$$

IV. Results

The theoretical model is a simple delta wing configuration with a leading-edge sweep of 45 deg and constructed from a 0.147-cm-thick plastic (Lucite®). The root chord is locally clamped (cantilevered), and the length of the cantilever root is 22.86 cm (60% root chord). The clamping is symmetric about the center of the root chord of the model. The length of the root chord is 38.1 cm. We use the aerodynamic vortex lattice model including 120 vortex elements on the delta wing ($km = kn = 15$), 525 vortex elements in the wake ($kmm = 50$), and nine reduced aerodynamic eigenmodes $R_a = 9$. The delta wing structural modal numbers are $nxy = 10$ in the out-of-plane and $mxy = 200$ in the in-plane directions, respectively. The mesh of the finite element model for the out-of- and in-plane structural model is 30×30, and thus the delta wing is modeled by using 900 quadrilateral plate elements. The nodes at the clamped root chord satisfy geometric boundary conditions, i.e., $w = u = v = \theta_x = \theta_y = \theta_z = 0$.

The store is a slender body attached at the fore and aft support points of the delta wing. The slender body is an aluminum tube, 1.59 cm in outside diameter and 12.7 cm in length. A paraboloidal forebody with 2.54-cm length is fixed to the fore end of the tube. The geometry of the paraboloidal forebody is described as follows:

$$R/R_0 = \bar{x}_{SB}^2, \qquad \bar{x}_{SB} = 0 \longrightarrow 1$$

The slender body is symmetrical. The distance between the fore and aft attachment points is $e_2 = 9.84$ cm; $J_\beta = 0.3686E_{-4}$ Nms^2, and $k_s = 36$ N/m. As shown in Fig. 1, $e_1 = 12.7$ cm, $e_3 = -0.23$ cm. $M_1 = 0.037$ kg, and $M_2 = 0.004$ kg. As shown in Eqs. (8-1) and (11-1),

$$\int_0^{c_{SB}} S dx_\beta = 2.715E^{-5} \text{ m}^3$$

$$\int_0^{c_{SB}} S[x_\beta - e_1]dx_\beta = 3.941E^{-7} \text{ m}^4$$

$$\int_0^{c_{SB}} S[x_\beta - e_1]^2 dx_\beta = 8.38E^{-8} \text{ m}^5$$

Two cases are considered. One is the "leading-edge" case. The fore attachment point (p_1 in Fig. 1) of the wing/store varies along the leading edge of the wing from the nondimensional span $y/c = 0$ (the root chord) to $y/c = 0.7$, and the store chord is always parallel to the root chord. The other is the "trailing-edge" case. The aft attachment location (p_2 in Fig. 1) of the wing/store varies along the trailing edge of the wing, and the store chord is always parallel to the root chord.

A. Results for the Linear System

1. *Wing/Store Structural Dynamic Behavior*

In the following calculation we consider the wing/store structural dynamic behavior of a linear system; i.e., the geometric structural nonlinearity of the wing is neglected. In computing the wing/store structural natural frequency, we use two distinct methods. One is a finite element method using a standard code, ANSYS. The finite element model has 721 nodes. The other is a component modal analysis as presented in this paper. Only the first 10 wing plate eigenmodes are taken into account in the calculations (of the total of 961 eigenmodes). The wing/store structural natural frequency varies with the different points of attachment of wing/store for the leading-edge case. Results are shown in Fig. 3 for the first four wing/store structural natural frequencies vs the nondimensional span location of the store attachment. In this case, the frequencies decrease when the store moves from the root to tip of the wing for the first two frequencies and also the fourth frequency. The results from the ANSYS analysis and the component mode analysis are in good agreement. Figure 4 shows the calculated node lines of the first four modes for $y/c = 291$. The first mode is dominated by the first wing bending mode. The second is dominated by the first torsion mode (note that the store pitch natural frequency alone is 15.5 Hz, which is close to the second wing/store natural frequency). The third is dominated by the first wing torsion mode, which is close to the second wing natural frequency (17.84 Hz) alone. The fourth is essentially the second wing bending mode. The overall agreement between the results from the finite element model (ANSYS code) and the component modal analysis is good.

2. *Flutter Behavior*

The flutter stability of the linearized aeroelastic wing/store model is determined by solving Eq. (33) when the gravity force F_g and F_N^p are neglected. (The wing is vertically mounted in the wing tunnel.) The aeroelastic eigenvalues obtained from these equations determine the stability of the system. When the real part of any one eigenvalue λ (damping) becomes positive, the entire system becomes unstable.

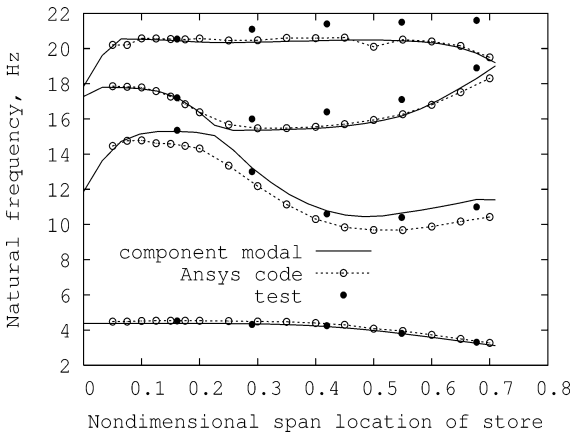

Fig. 3 Wing/store structural natural frequencies vs the nondimensional span location of store attachment for the first four modes.

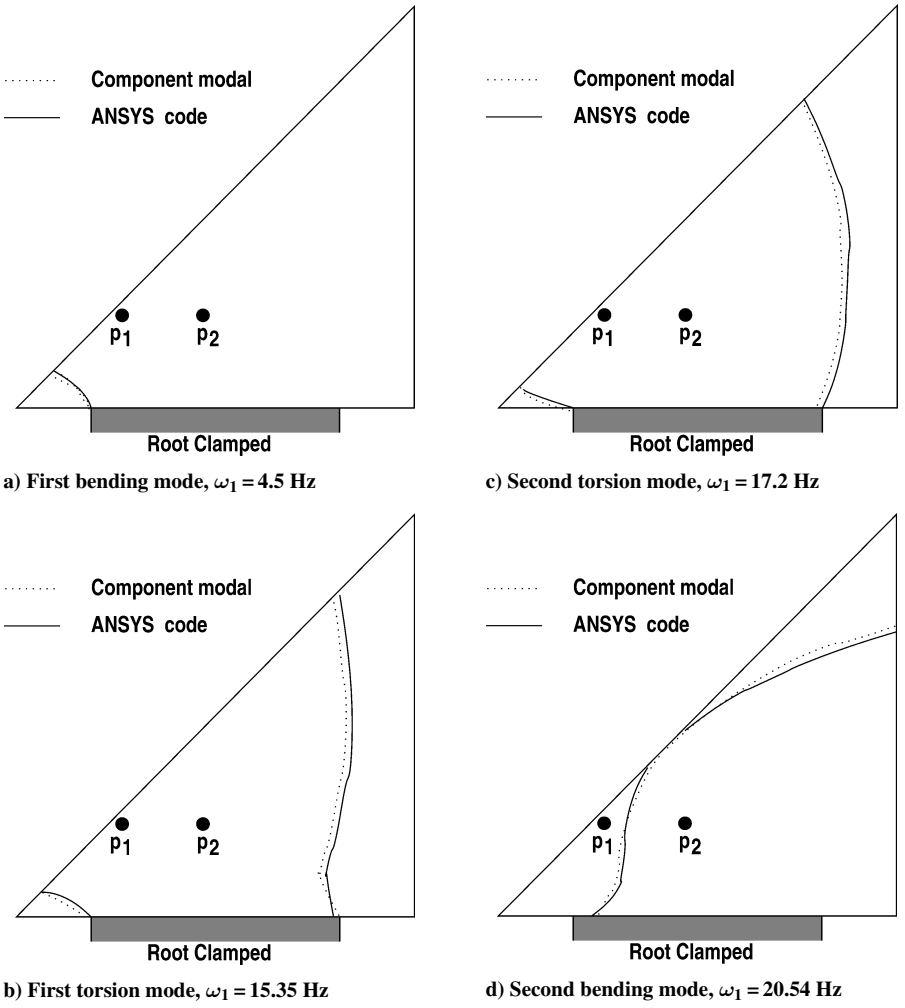

a) First bending mode, $\omega_1 = 4.5$ Hz **c) Second torsion mode, $\omega_1 = 17.2$ Hz**

b) First torsion mode, $\omega_1 = 15.35$ Hz **d) Second bending mode, $\omega_1 = 20.54$ Hz**

Fig. 4 Node lines of the first four modes for a nondimensional span location of store attachment of 0.291; p_1 and p_2 are the fore and aft attachment points between the wing and store.

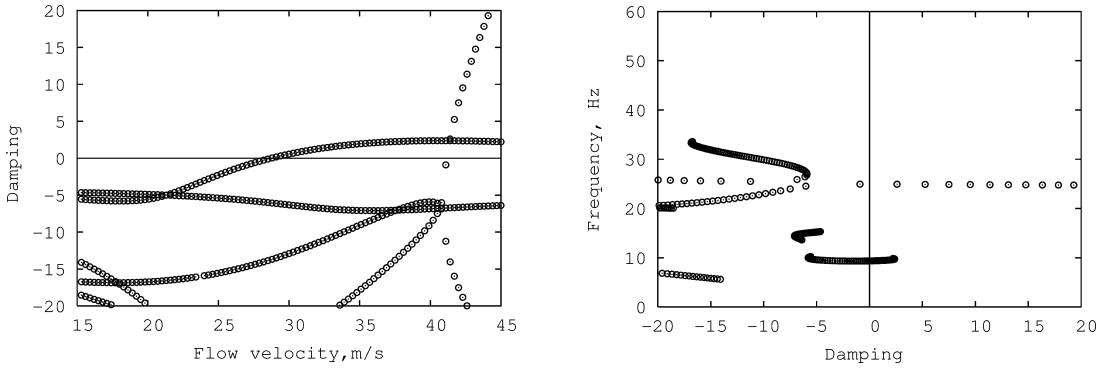

a) Real part **b) Root locus**

Fig. 5 Graphical representation of the eigenanalysis for $y/c = 0.419$, $k_s = 36$ N/m, and the leading-edge case.

Figure 5 shows a typical graphical representation of the eigenanalysis in the form of the real part of the eigenvalues $\mathrm{Re}(\lambda_i)$ (damping) vs the flow velocity and also a root-locus plot for $y/c = 0.419$ and the leading-edge case. As indicated by the symbol $\circ$, there are two types of flutter modes. For the first flutter mode, there is an intersection with the velocity axis at $U_f = 28.8$ m/s and the corresponding flutter oscillatory frequency is $\omega_f = 9.35$ Hz. For the second flutter mode, there is an intersection with the velocity axis at $U_f = 41.5$ m/s and the corresponding flutter oscillatory frequency is $\omega_f = 25$ Hz. As shown in the root-locus plot of Fig. 5b, the first flutter mode is dominated by the second wing/store mode, i.e, the coupling of the first (first bending) and second (first torsion) modes of the wing/store system. The second flutter mode is dominated by the third wing/store mode, i.e., the coupling of the third (second torsion) and fourth (second bending) modes of the wing/store system. Although there are two flutter velocities, $U_f = 28.8$ and 41.5 m/s, the lowest flutter velocity (determining the critical flutter boundary) is due to the first flutter mode.

Effect of store pitch stiffness. The effects of the store pitch stiffness (store attachment stiffness) on the flutter boundary are

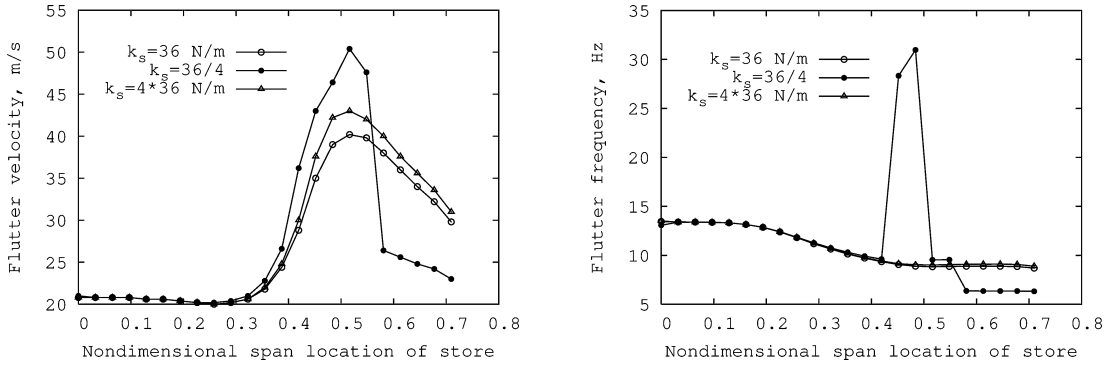

a) Flutter velocity **b) Flutter frequency**

Fig. 6 Flutter velocity and frequency vs nondimensional span location of store for leading-edge case.

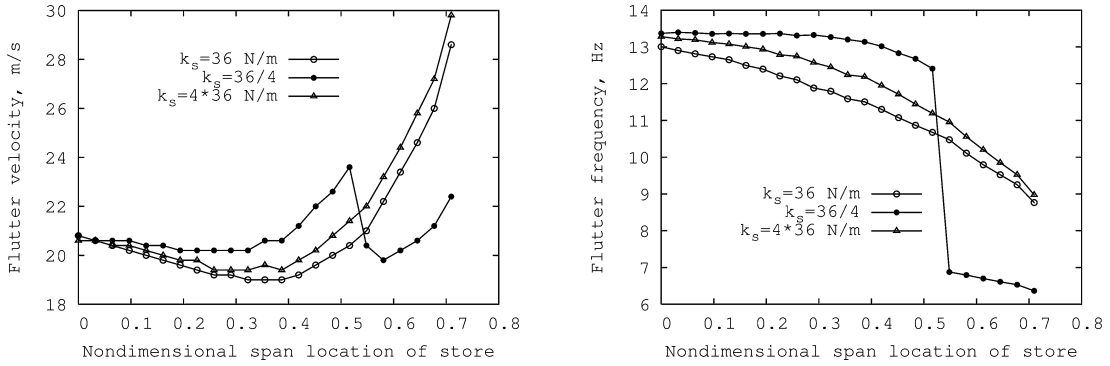

a) Flutter velocity **b) Flutter frequency**

Fig. 7 Flutter velocity and frequency vs nondimensional span location of store for trailing-edge case.

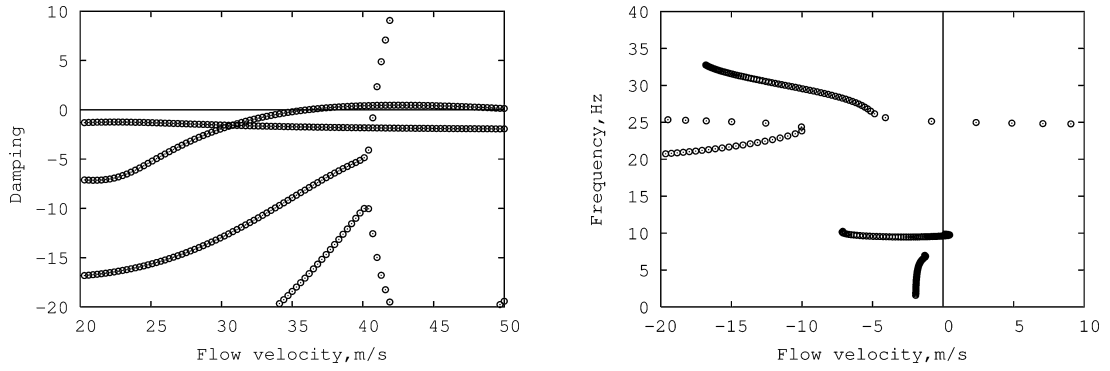

a) Real part **b) Root locus**

Fig. 8 Graphical representation of the eigenanalysis for $y/c = 0.419$, $k_s = 36/4$ N/m, and the leading-edge case.

considered next. The nominal pitch stiffness is $k_s = 36$ N/m, and the pitch natural frequency $\omega_\beta = 15.5$ Hz. Two additional pitch stiffness are considered: $k_s = 36/4$ N/m, $\omega_\beta = 7.75$ Hz and $k_s = 4 \times 36$ N/m, $\omega_\beta = 31$ Hz. The flutter velocities vs nondimensional span location of the store are shown in Fig. 6a for the leading-edge case and Fig. 7a for the trailing-edge case. The corresponding flutter oscillatory frequencies are shown in Figs. 6b and 7b, respectively.

For the leading-edge case, the effects of the store attachment stiffness are small for the store location $y/c < 0.3$. A significant effect occurs when the nondimensional store location is larger than 0.4, especially for the smaller pitch stiffness. When the pitch stiffness of the store is larger, $k_s = 4 \times 36$ N/m, the critical flutter boundary is a little higher than that for the nominal pitch stiffness over all store locations. The critical flutter mode is dominated by the coupled first bending and first torsion modes for both $k_s = 36$ and 4×36 N/m.

When the pitch stiffness of the store is smaller, $k_s = 36/4$ N/m, the critical flutter boundary is higher for $0.516 > y/c > 0.4$ and smaller for $y/c > 0.58$. There is a flutter "jump" phenomenon at $y/c = 0.548$, as shown in Fig. 6a. Three flutter modes are found. The first flutter mode is dominated by the second wing/store mode (coupled by the first bending and first torsion modes). The second flutter mode is dominated by the third wing/store mode (coupled by the second torsion and second bending modes). The third flutter mode is dominated by the first wing/store mode (coupled by the first bending and first torsion modes). As shown in Fig. 6b, there are three jump frequencies at $y/c = 0.419$, 0.484, and 0.548. The flutter boundary and flutter mode do depend on the position of the store for the lower pitch stiffness of the store.

For the same case, Fig. 8 shows a graphical representation of the eigenanalysis for $y/c = 0.419$. There are three flutter velocities,

$U_f = 36.5$, 40.5, and 50 m/s, and the corresponding flutter oscillatory frequencies are $\omega_f = 9.62$, 25, and 10 Hz. The lowest flutter velocity (critical flutter boundary) is $U_f = 36.5$ m/s and corresponds to a "hump" flutter mode. Comparing Fig. 8 to Fig. 5 for the same span location of store, $y/c = 0.419$, but with a different store pitch stiffness, we can define two quantities to describe their distinctive behavior. One is a hump flutter "strength," which is defined as the maximum "positive" aeroelastic damping, $\xi_f = \mathrm{Re}(\lambda)|_{\max}$, in the range of the hump flutter mode. The other is a flutter mode separation coefficient $\Delta\bar{U}_f$, which is defined as the relative flutter velocity difference between the first and second flutter velocities, i.e., $\Delta\bar{U}_f = (U_{f2} - U_{f1})/U_{f1}$. For the case of the small store pitch stiffness as shown in Fig. 8, both the hump flutter strength and the flutter mode separation coefficient are much smaller than those for $k_s = 36$ N/m. For $U_{f1} = 36.5$ m/s and $U_{f2} = 40.5$ m/s, $\Delta\bar{U}_f = 0.108$ and the hump flutter strength $\xi_f = 0.28$ for $k_s = 36/4$ N/m. See Fig. 8. For U_{f1} and U_{f2} equal to 28.8 and 41 m/s, $\Delta\bar{U}_f = 0.42$ and the hump flutter strength $\xi_f = 2.72$ for $k_s = 36$ N/m. See Fig. 5. These results affect the LCO behavior as discussed in the next section.

For the trailing-edge case, the results are shown in Fig. 7. For the smaller store pitch stiffness, the critical flutter velocity is higher for $y/c < 0.516$, and also there is a flutter velocity and frequency jump at $y/c = 0.516$. A typical graphical representation of the eigenanalysis in the form of the real part of the eigenvalues $\mathrm{Re}(\lambda_i)$ (damping) vs the flow velocity and also a root-locus plot for $y/c = 0.516$ is shown in Fig. 9. There are three flutter velocities, $U_f = 20.5$, 28, and 28.2 m/s, and the corresponding flutter oscillatory frequencies are $\omega_f = 6.8$, 12, and 6.85 Hz. The critical flutter boundary is associated with a hump flutter mode, which is dominated by the second wing/store mode, i.e., the coupling of first bending and first torsion modes of the wing/store system. The second flutter mode is dominated by the third wing/store mode, i.e., the coupling of first bending and second torsion modes of the wing/store system.

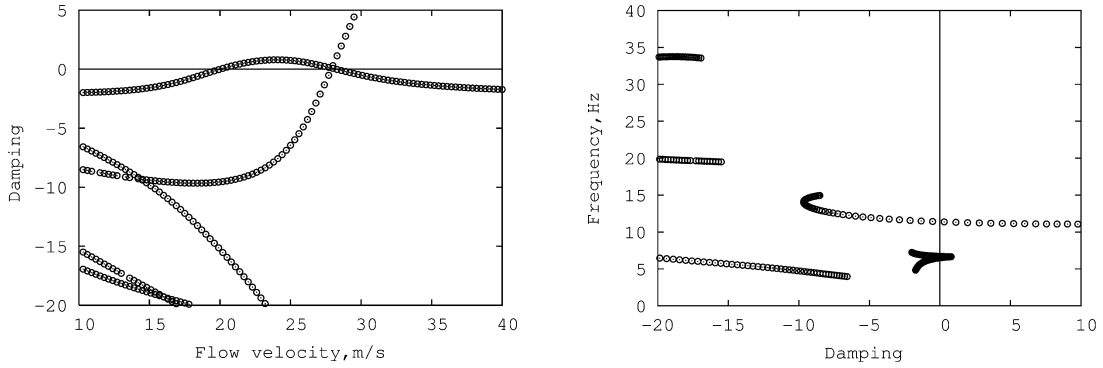

a) Real part **b) Root locus**

Fig. 9 Graphical representation of the eigenanalysis for $y/c = 0.548$, $k_s = 36/4$ N/m, and the trailing-edge case.

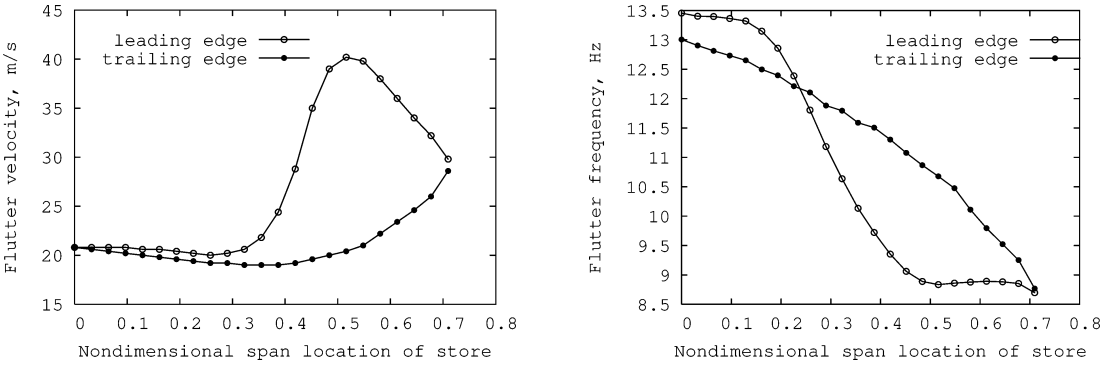

a) Flutter velocity **b) Flutter frequency**

Fig. 10 Flutter velocity and frequency vs nondimensional span location of store and $k_s = 36$ N/m.

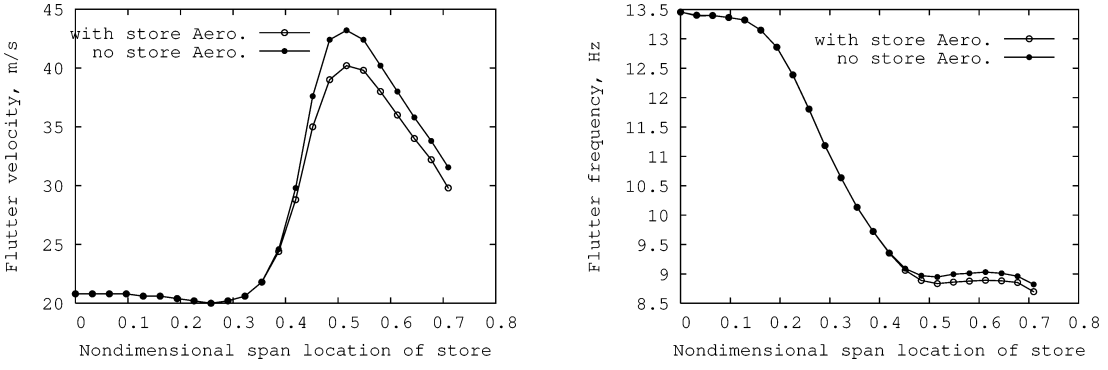

a) Flutter velocity **b) Flutter frequency**

Fig. 11 Flutter velocity and frequency vs nondimensional span location of the store for the nominal pitch stiffness and the leading-edge case with and without store aerodynamics.

Effect of store location. The effects of the store location on the flutter are now considered. The results for both the leading edge and trailing-edge cases are shown in Fig. 10 for the nominal pitch stiffness. The critical flutter boundary for the leading-edge case is higher than that for the trailing-edge case over all of the store span locations. The minimum and maximum for the flutter boundaries are located at $y/c = 0.258$ and 0.516, respectively, for the leading-edge case and 0.387 and 0.709 for the trailing-edge case. For the other pitch stiffnesses, the results are shown in Figs. 6 and 7. It is seen that the critical flutter boundary and frequency are sensitive to the span location of the store. For the present wing/store model, if the store is placed near the midspan at the leading edge, the system has a maximum critical flutter boundary that is independent of the store pitch stiffness.

Effect of store aerodynamics. Now considered are the effects of the store aerodynamic force on the flutter. Unsteady slender-body aerodynamic theory is used in the calculations as a first approximation. Nominal pitch stiffness and the leading-edge case are considered. Figure 11a shows the critical flutter boundary vs the nondimensional span location of the store, and Fig. 11b shows the corresponding flutter frequency. When the store is located near the root, the effects of the store aerodynamic force are very small, but for locations near the wing tip the effects are significant. The effect of the store aerodynamic force is to reduce the critical flutter boundary. The effects on the flutter frequency are small.

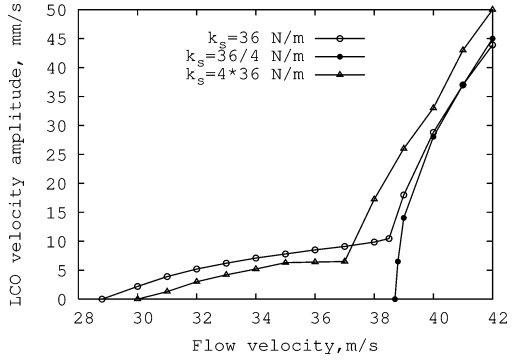

a) LCO midwing response

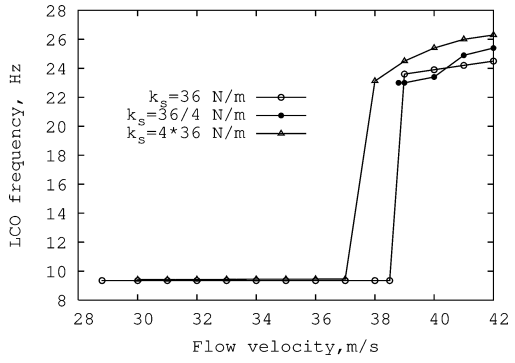

b) LCO frequency

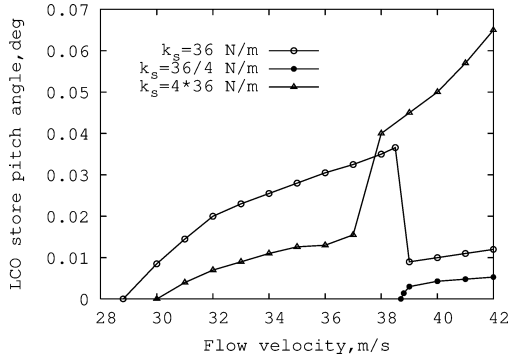

c) LCO store pitch response

Fig. 12 LCO behavior vs flow velocity for *y/c* = 0.419 and the leading-edge case.

B. Results for the Nonlinear System

In the following calculations we consider only the geometric structural nonlinearity of the wing. LCO phenomena are observed when the flow velocity is higher than the critical flutter velocity. The LCO behavior depends on the flutter mode. First considered are the effects of varying the pitch stiffness of the store on the LCO behavior. Subsequently the influence of the position of the store is considered.

Effect of store pitch stiffness. Figure 12a shows the typical LCO rms velocity amplitude at the wing midspan of the trailing edge vs the flow velocity for $y/c = 0.419$ and the leading-edge case. The corresponding LCO frequency and store pitch amplitude results are shown in Figs. 12b and 12c. Three store pitch stiffnesses are considered. For $k_s = 36$ N/m and $k_s = 4 \times 36$ N/m, there is a jump phenomenon at a flow velocity of $U = 39.25$ and 37 m/s, respectively. The LCO response is influenced by two flutter modes. Before the jump velocity, the LCO response is dominated by the first flutter mode; see Fig. 5. The LCO frequency is close to the flutter frequency of the first flutter mode, and the frequency is almost independent of the flow velocity as shown in Fig. 12b. After the jump velocity the LCO response is dominated by the second flutter mode; also see Fig. 5. The LCO frequency is near the second flutter mode frequency, and the frequency, increases as the flow velocity increases.

A typical response time history at midspan of the leading edge for $U = 38$ m/s is shown in Fig. 13a. The motion is a single harmonic oscillation due to the first flutter mode. The rms amplitude described in Fig. 12 is obtained from the steady-state time history (after 6 s) as shown in Fig. 13a. Figure 13b shows the fast Fourier transform (FFT) analysis of the midspan velocity responses for $U = 38, 39$, and 41 m/s. (The time histories are not shown for $U = 39$ and 41 m/s.) At $U = 38$ m/s, the motion is nearly single harmonic (first flutter mode). At $U = 41$ m/s, the motion is dominated by the second flutter mode; the effect of the first flutter mode is much smaller. At $U = 39$ m/s, the motion is dominated by the second flutter mode, but the effect of the first flutter mode is still detectable.

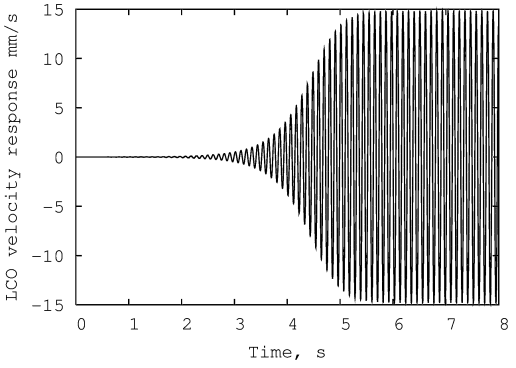

a) Time history, *U* = 38 m/s

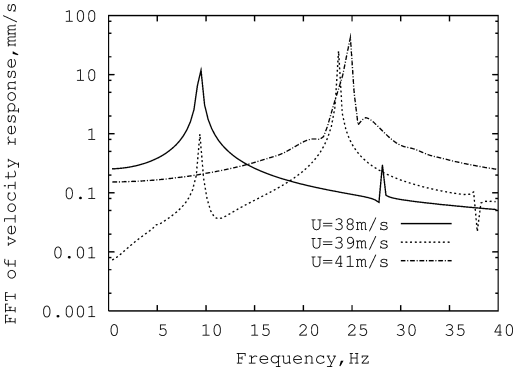

b) FFT analysis

Fig. 13 Time history and FFT analysis for *y/c* = 0.419 and the leading-edge case.

For $k_s = 36/4$ N/m, the LCO response is dominated by the second flutter mode and the first flutter mode disappears. Recall Fig. 8; the critical flutter boundary is 36.5 m/s, and the second flutter velocity is 40.5 m/s. There are two key questions: Why does the first flutter mode disappear? Why does LCO occur at about $U = 39$ m/s rather than at $U = U_f = 40.5$ m/s? One explanation is that the onset of the LCO depends on the structural nonlinearity, the linear flutter strength ξ_f, and the flutter mode separation coefficient $\Delta\bar{U}_f$. In the present case, the flutter strength is very weak ($\xi_f = 0.28$) for the first flutter mode and relatively strong for the sencond flutter mode. The flutter mode separation coefficient is very small ($\Delta\bar{U}_f = 0.108$). The structural nonlinearity can easily change the original linear flutter state and allow the LCO to be dominated by the second flutter mode.

Figure 12c shows the typical LCO store pitch response for several different pitch stiffnesses. The store pitch response is relatively small.

Effect of store location. The effects of the store location on the LCO behavior are also considered. Five span locations of the store for the leading-edge case are chosen to calculate the LCO response: $y/c = 0.161$, 0.291, 0.419, 0.548, and 0.677. The results are shown in Fig. 14 for the nominal pitch stiffness. The LCO behavior varies with the store location and depends on the linear flutter mode.

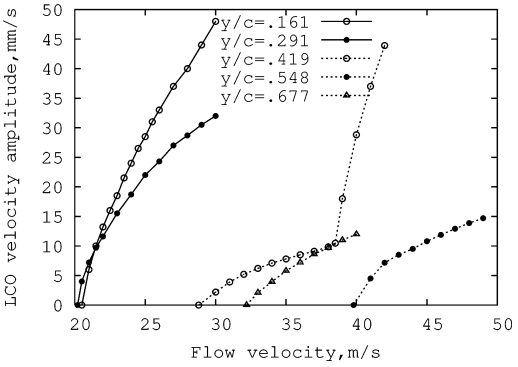

a) LCO midwing response

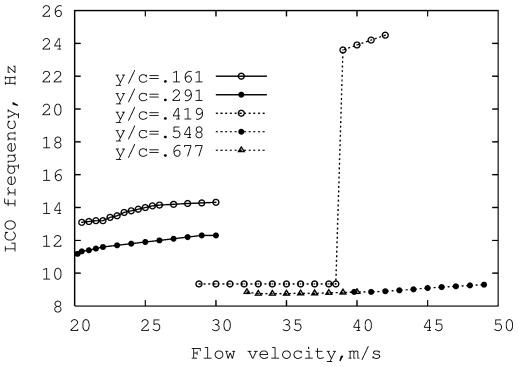

b) LCO frequency

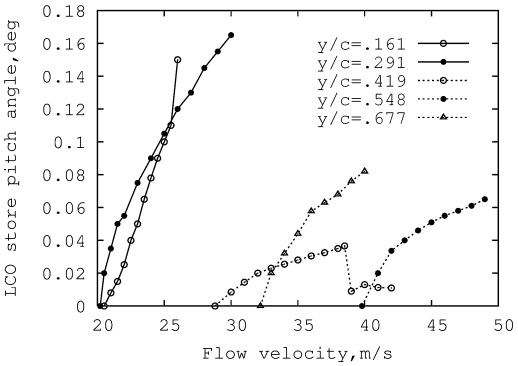

c) LCO store pitch response

Fig. 14 LCO behavior vs flow velocity for $k_s = 36$ N/m and several store locations and the leading-edge case.

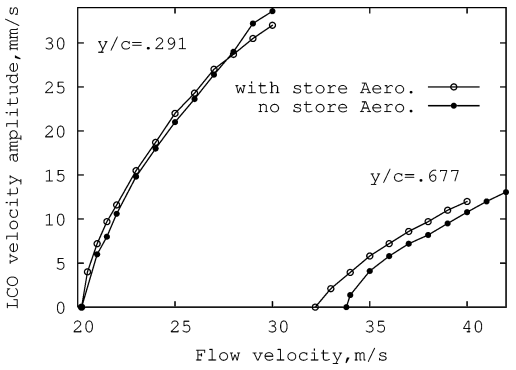

a) LCO midwing response

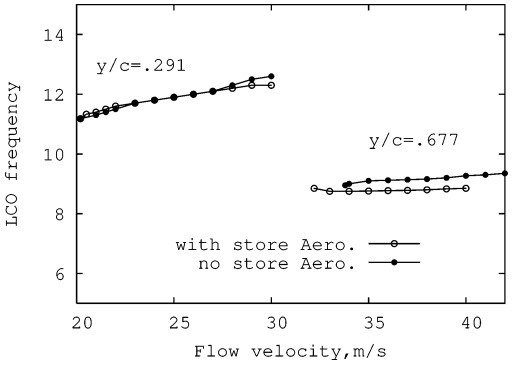

b) LCO frequency

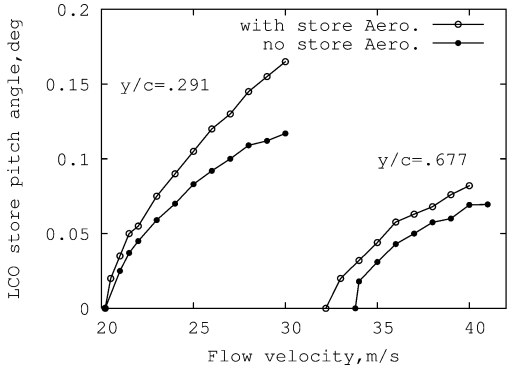

c) LCO store pitch response

Fig. 15 LCO behavior vs flow velocity for $k_s = 36$ N/m, store locations $y/c = 0.291$ and 0.677, and the leading-edge case with and without store aerodynamics.

Effect of store aerodynamics. Now considered are the effects of the store aerodynamic force on the LCO behavior. Two store span locations and the leading-edge case are used in the calculations. Nominal pitch stiffness is considered. Figure 15a shows the LCO velocity amplitude vs the flow velocity for $y/c = 0.291$ and 0.677. When the store is located near the wing root, such as $y/c = 0.291$, the effects of the store aerodynamic force on the wing LCO behavior are very small for both LCO amplitude and frequency, as shown in Figs. 15a and 15b. But it influences the store pitch response, as shown in Fig. 15c. The unsteady slender-body aerodynamics lead to an increase in the store pitch response as the flow velocity increases.

When the store is located near the wing tip, such as $y/c = 0.677$, the effects of the store aerodynamic force are relatively larger for both response amplitude and frequency. This effect is due to the change in the critical flutter boundary.

Finally the interesting work of Thompson and Strganac and Beran et al. on wing/store flutter and LCO should be mentioned as described in two forthcoming papers.[11,12]

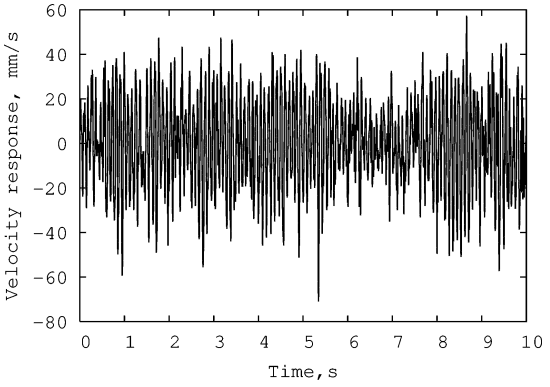

a) $U = 22.48$ m/s

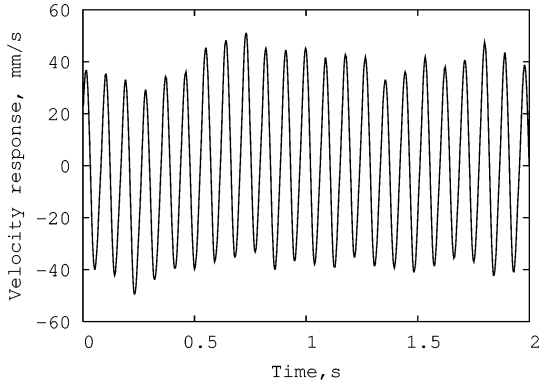

b) $U = 22.96$

Fig. 16 Measured time histories from the midspan of the trailing edge for $y/c = 0.291$ and the leading-edge case.

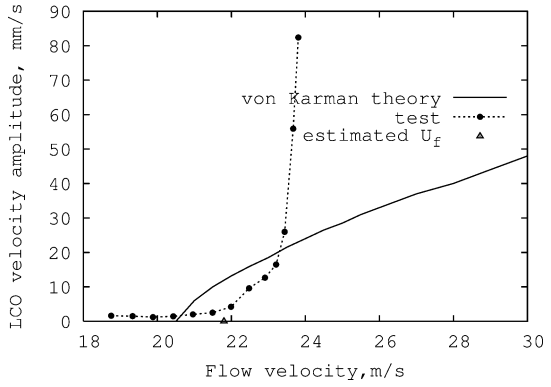

a) LCO midwing response

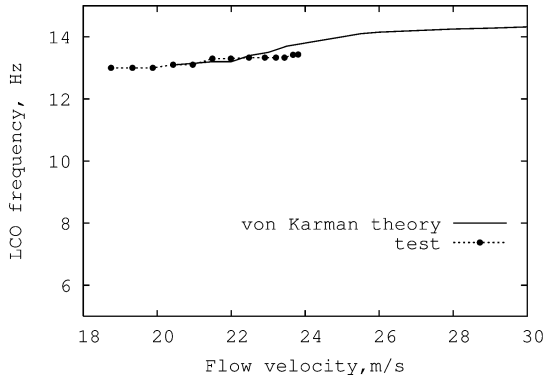

b) LCO frequency

Fig. 18 LCO behavior vs flow velocity for $k_s = 36$ N/m and store location, $y/c = 0.161$ and the leading-edge case.

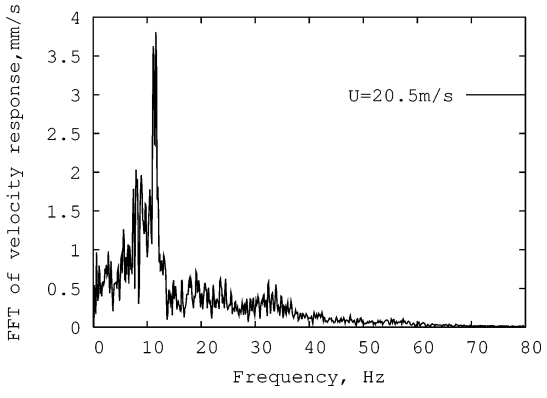

a) $U = 20.5$ m/s

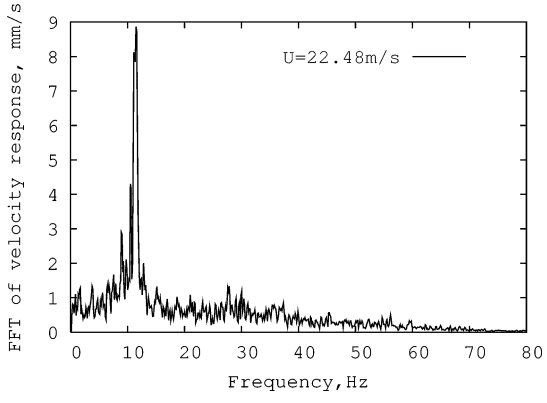

c) $U = 22.48$ m/s

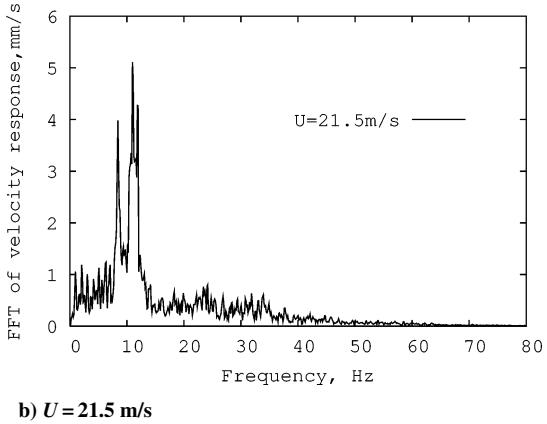

b) $U = 21.5$ m/s

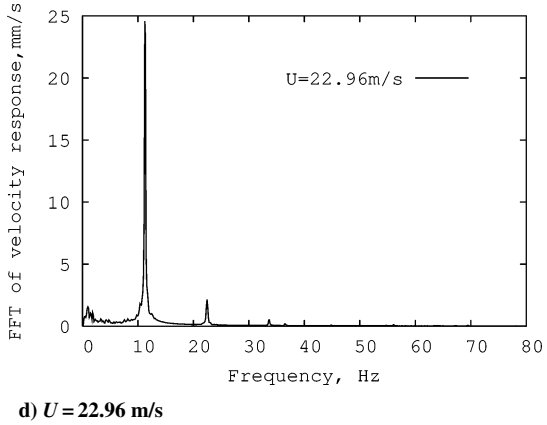

d) $U = 22.96$ m/s

Fig. 17 FFT analysis of LCO velocity response measured from the midspan of the trailing edge of the store for $y/c = 0.291$.

V. Theoretical and Experimental Flutter Correlations

The experimental delta wing and the store configurations are the same as for the theoretical model. The store pitch stiffness k_s is 36 N/m, and the corresponding store pitch natural frequency is 15.5 Hz. The first five natural frequencies of the delta wing plate alone are 4.39, 17.84, 20.62, 42.21, and 51.87 Hz. These results are obtained from a finite element method using a standard code, ANSYS. Five span locations of the store for the leading-edge case are considered in the experiment: $y/c = 0.161, 0.291, 0.419, 0.548$, and 0.677.

To check the wing/store structural dynamic behavior, a vibration test for the wing/store model is made. The natural frequencies are determined by measuring the transfer function of input force and output acceleration. A force transducer B&K 8200 fixed near the wing root is excited by a minishaker B&K 4810 and a power amplifier B&K 2706. A four-channel signal analyzer (SD 380) provides a sweeping sinusoidal signal. The output signal from a microaccelerometer (at wing tip) provides inputs to the SD380 for transfer function analysis. The experimental results for the first four natural frequencies are shown in Fig. 3 as indicated by the symbol •. The agreement for the first two natural frequencies is excellent and for the third and fourth natural frequencies is reasonably good.

An Ometron VPI 4000 Scanning Laser Vibrometer system is used to measure the velocity deflection at the midspan of the trailing edge. The LCO velocity responses vs the flow velocity are measured for the five span locations of the store mentioned earlier. The sampling rate is 500 points/s, $\Delta t = 1/500$, and the total sampling length is 5000 points. An ensemble averaged FFT analysis is used to determine LCO velocity amplitude and frequency by using a time delay average method. The delay time is $2 \times \Delta t$, and the FFT analysis uses 2048 sampling points. The ensemble average number is 100. Typical measured time histories are shown in Figs. 16a and 16b for $y/c = 0.291$ and flow velocity $U = 22.48$ and 22.96 m/s. Figure 16b is taken over the first 2 s from the total sampling length. It is found that the measured time history is not a pure harmonic motion as predicted by the theory. There are some beat motions and higher harmonic responses in this time history. An ensemble averaged FFT analysis is necessary to describe the LCO behavior.

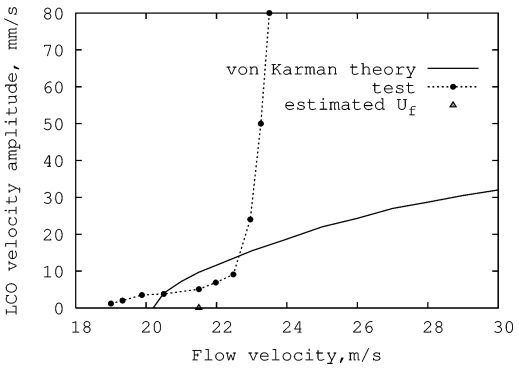

a) LCO midwing response

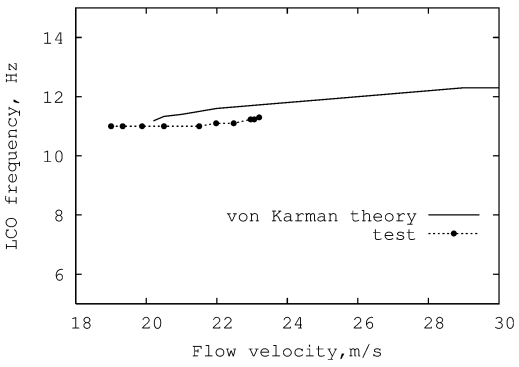

b) LCO frequency

Fig. 19 LCO behavior vs flow velocity for $k_s = 36$ N/m and store location, $y/c = 0.291$ and the leading-edge case.

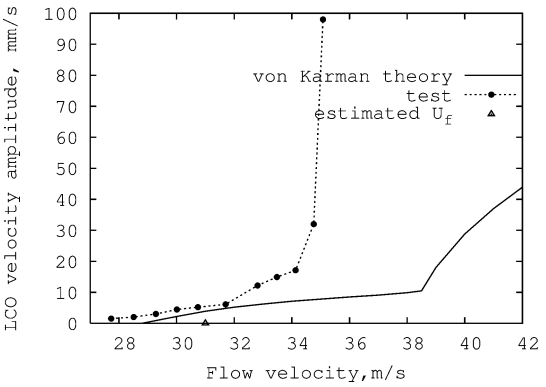

a) LCO midwing response

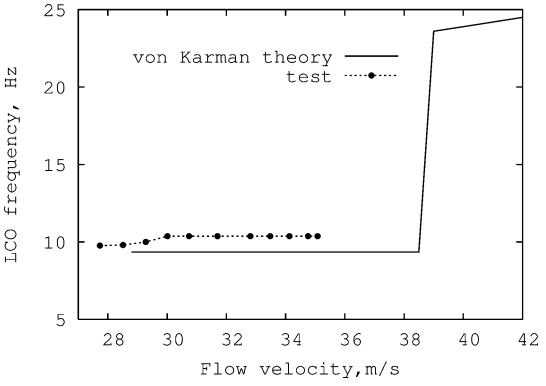

b) LCO frequency

Fig. 20 LCO behavior vs flow velocity for $k_s = 36$ N/m and store location, $y/c = 0.419$ and the leading-edge case.

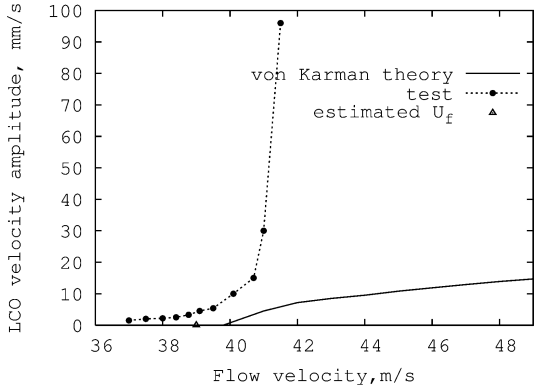

a) LCO midwing response

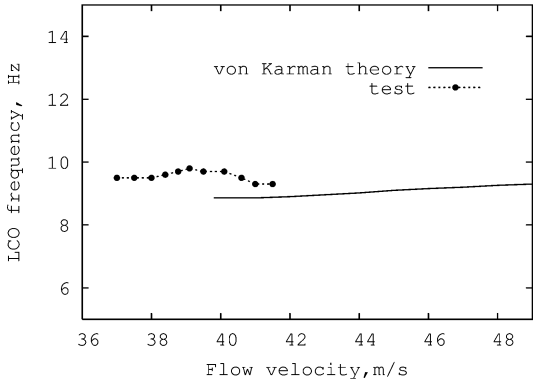

b) LCO frequency

Fig. 21 LCO behavior vs flow velocity for $k_s = 36$ N/m and store location, $y/c = 0.548$ and the leading-edge case.

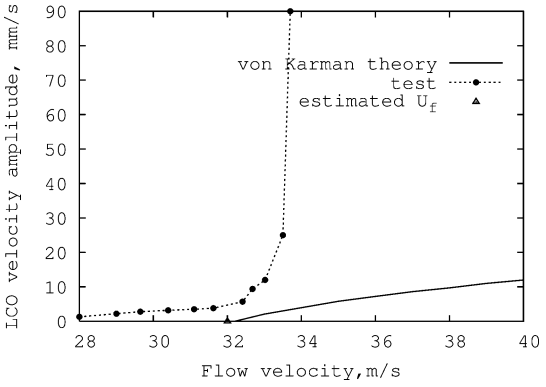

a) LCO midwing response

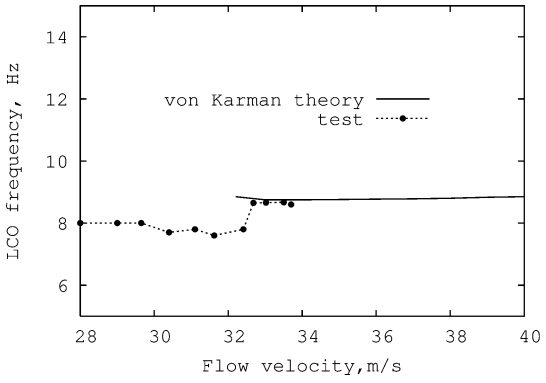

b) LCO frequency

Fig. 22 LCO behavior vs flow velocity for $k_s = 36$ N/m and store location, $y/c = 0.677$ and the leading-edge case.

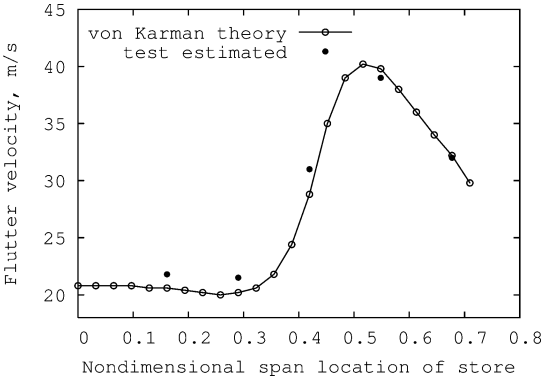

a) Flutter velocity

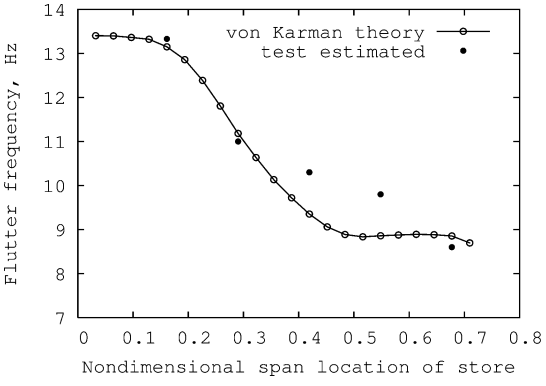

b) Flutter frequency

Fig. 23 Flutter velocity and frequency vs nondimensional span location of the store for the nominal pitch stiffness and the leading-edge case.

The FFT analysis of a typical measured signal vs the flow velocity is shown in Figs. 17a–17d for a flow velocity from 20.15 to 22.96 m/s and $y/c = 0.291$. LCO are observed in this range of flow velocities. As shown in Fig. 17c, the LCO amplitude is 9.1 mm/s and the LCO frequency is 11.1 Hz for $U = 22.48$ m/s. This is essentially a single harmonic oscillation with some background noise. As the flow velocity decreases, the frequency response component at about 11 Hz decreases and there are some other small-amplitude frequency components, as shown in Figs. 17a and 17b. As the flow velocity increases from $U = 22.48$ m/s, the main frequency response component (about 11 Hz) abruptly increases and there are some second and third harmonic frequency components, as shown in Fig.17d. The linear critical flutter velocity is thought to be near this flow velocity.

Figures 18–22 show the theoretical and experimental correlations of the LCO velocity response rms amplitude and LCO frequency for y/c from 0.161 to 0.677. Each experimental data point is obtained from the ensemble averaged FFT analysis, and only the main frequency component is taken from the FFT plot. When the store location is near the wing root, as shown in Figs.18 and 19, the correlation between the theory and experiment is reasonably good in the lower-flow-velocity range. For the higher-flow-velocity range, there is a large difference between the theory and experiment for the LCO amplitude. When the store location is near the wing tip, as shown in Figs. 21 and 22, the correlation between the theory and experiment for LCO amplitude is poor. The von Kármán plate theory seems inadequate to describe the structural nonlinear characteristics of the present experimental model.

The linear critical flutter boundary is estimated from Figs. 18–22. An intersection between the extrapolated LCO amplitude curve and the flow velocity axis is defined as the linear critical flutter boundary. This estimated value is also plotted in Figs. 18–22 as indicated by the symbol $\triangle$.

Figure 23a shows the theoretical and experimental (estimated) critical flutter boundary vs the nondimensional span location of the store in the leading-edge case. Figure 23b shows the corresponding flutter frequency. The correlations between the theory and experiment are better for the flutter boundary than for the LCO behavior.

VI. Conclusions

The flutter and LCO behavior of a delta wing with an external store model are studied by using von Kármán plate theory, a component modal analysis, and a three-dimensional time domain vortex lattice aerodynamic model including a reduced-order model aerodynamic technique. Results are computed for different store span locations, different store pitch stiffnesses, and with/without store aerodynamics.

It is found that the flutter and LCO behavior is sensitive to the store span location and store attachment stiffness, especially when the store is near the wing tip. Comparing the leading-edge case to the trailing-edge case, the former has a higher critical flutter velocity. For a lower store attachment stiffness, i.e., the store pitch natural frequency is near the first wing natural frequency, the flutter mode becomes complex. Some very low flutter velocities may occur for certain store span locations.

The theoretical results are compared to experiment. The correlations between the theory and experiment are good for both the critical flutter velocity and frequency but not good for the LCO amplitude, especially when the store is located near the wing tip. The theoretical model needs to be improved to determine LCO response, and improved results are shown in the companion paper as obtained by using a higher-order structural theory.

Acknowledgments

This work was supported under Air Force Office of Scientific Research Grant "Dynamic and Control of Nonlinear Fluid-Structure Interaction" under the direction of Dean Mook and Tom Kim.

References

[1]Doggett, R.V., and Solstmann, D. L., "Some Low-Speed Flutter Characteristics of Simple Low-Aspect-Ratio Delta Wing Models," NASA TM 101547, Jan. 1989.

[2]Tang, D. M., Henry, J. K., and Dowell, E. H., "Limit Cycle Oscillations of Delta Wing Models in Low Subsonic Flow," *AIAA Journal*, Vol. 37, No. 11, 1999, pp. 1355–1362.

[3]Tang, D. M., and Dowell, E. H., "Effects of Steady Angle of Attack on Nonlinear Flutter of a Delta Wing Plate Model," *Journal of Aircraft*, Vol. 39, No. 1, 2001, pp. 15–21.

[4]Attar, P. J., Dowell, E. H., and Tang, D. M., "A Theoretical and Experimental Investigation of the Effects of a Steady Angle of Attack on the Nonlinear Flutter of a Delta Wing Plate Model," *Journal of Fluids and Structures*, Vol. 17, No. 2, 2003, pp. 243–259.

[5]Gordnier, R. E., "Computation of Limit Cycle Oscillations of a Delta Wing," AIAA Paper 2002-1411, April 2002.

[6]Dowell, E. H., and Tang, D. M., *Dynamics of Very High Dimensional Systems*, World Scientific, Singapore, 2003, Chap. 10.

[7]Tongue, B. H., and Dowell, E. H., "Component Mode Analysis of Nonlinear, Nonconservative Systems," *Journal of Applied Mechanics*, Vol. 50, March 1983, pp. 204–209.

[8]Dowell, E. H., and Hall, K. C., "Modeling of Fluid-Structure Interaction," *Annual Review of Fluid Mechanics*, Vol. 33, 2001, pp. 445–490.

[9]ANSYS User Manual, Release 5.5.1, Swanson Analysis Systems, Inc., Houston, TX, 1998.

[10]Bisplinghoff, R. L., Ashley, H., and Halfman, R. L., *Aeroelasticity*, Addison Wesley, New York, 1955, pp. 418–436.

[11]Thompson, D. E., Jr., and Strganac, T. W., "Nonlinear Analysis of Store-Induced Limit Cycle Oscillations," *Nonlinear Dynamics* (to be published).

[12]Beran, P. S., Strganac, T. W., Kim, K., and Nichkawde, C., "Studies of Store-Induced Limit Cycle Oscillations Using a Model with Full System Nonlinearities," *Nonlinear Dynamics* (to be published).

E. Livne
Associate Editor